ACS NANO
Cite This: ACS Nano 2018, 12, 2569–2579
www.acsnano.org

ARTICLE

Tuning Electronic Structure of Single Layer MoS_2 through Defect and Interface Engineering

Yan Chen,[*,†,‡,¶,●] Shengxi Huang,[§,#,●] Xiang Ji,[‡] Kiran Adepalli,[‡] Kedi Yin,[▽] Xi Ling,[§,◆] Xinwei Wang,[○] Jianmin Xue,[▽] Mildred Dresselhaus,[§,∥] Jing Kong,[*,‡,§] and Bilge Yildiz[*,†,⊥]

[†]Department of Nuclear Science and Engineering, [‡]Research Laboratory of Electronics, [§]Department of Electrical Engineering and Computer Science, [∥]Department of Physics, and [⊥]Department of Material Science and Engineering, Massachusetts Institute of Technology, Cambridge, Massachusetts 02139, United States

[#]Department of Electrical Engineering, The Pennsylvania State University, University Park, Pennsylvania 16802, United States

[▽]State Key Laboratory of Nuclear Physics and Technology, School of Physics, Peking University, Beijing 100871, P. R. China

[○]School of Advanced Materials, Shenzhen Graduate School, Peking University, Shenzhen 518055, P. R. China

[◆]Department of Chemistry, Division of Materials Science and Engineering, and The Photonics Center, Boston University, Boston, Massachusetts 02215, United States

Supporting Information

ABSTRACT: **Transition-metal dichalcogenides (TMDs) have emerged in recent years as a special group of two-dimensional materials and have attracted tremendous attention. Among these TMD materials, molybdenum disulfide (MoS_2) has shown promising applications in electronics, photonics, energy, and electrochemistry. In particular, the defects in MoS_2 play an essential role in altering the electronic, magnetic, optical, and catalytic properties of MoS_2, presenting a useful way to engineer the performance of MoS_2. The mechanisms by which lattice defects affect the MoS_2 properties are unsettled. In this work, we reveal systematically how lattice defects and substrate interface affect MoS_2 electronic structure. We fabricated single-layer MoS_2 by chemical vapor deposition and then transferred onto Au, single-layer graphene, hexagonal boron nitride, and CeO_2 as substrates and created defects in MoS_2 by ion irradiation. We assessed how these defects and substrates affect the electronic structure of MoS_2 by performing X-ray photoelectron spectroscopy, Raman and photoluminescence spectroscopies, and scanning tunneling microscopy/spectroscopy measurements. Molecular dynamics and first-principles based simulations allowed us to conclude the predominant lattice defects upon ion irradiation and associate those with the experimentally obtained electronic structure. We found that the substrates can tune the electronic energy levels in MoS_2 due to charge transfer at the interface. Furthermore, the reduction state of CeO_2 as an oxide substrate affects the interface charge transfer with MoS_2. The irradiated MoS_2 had a faster hydrogen evolution kinetics compared to the as-prepared MoS_2, demonstrating the concept of defect controlled reactivity in this phase. Our findings provide effective probes for energy band and defects in MoS_2 and show the importance of defect engineering in tuning the functionalities of MoS_2 and other TMDs in electronics, optoelectronics, and electrochemistry.**

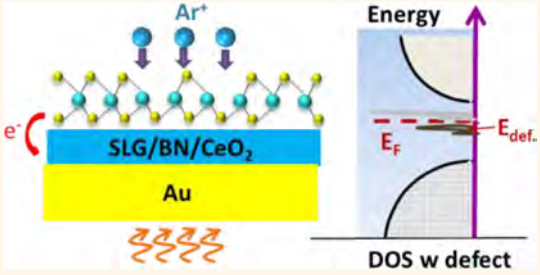

KEYWORDS: *transition-metal dichalcogenides, hydrogen evolution reaction, ion irradiation, X-ray photoelectron spectroscopy, Raman spectroscopy, scanning tunneling microscopy*

Molybdenum disulfide (MoS_2), a layered material in the family of transition-metal dichalcogenides (TMDs), has attracted tremendous attention in recent years due to its extraordinary performance in electronic transistors,[1,2] flexible and transparent displays,[3−5] optoelectronic devices,[2,4−7] sensors, and energy applications.[4,8] As a material with an extra-large surface-to-bulk ratio, single-layer (SL) MoS_2 is highly conducive to forming defects.[9] The defects in MoS_2 play an essential role in tuning the properties of SL MoS_2 in various ways and so affect the performance of devices based on MoS_2. They can, for example, enhance the electrochemical activity[10,11] and tune the electronic,[12] mag-

Received: November 27, 2017
Accepted: February 2, 2018
Published: February 3, 2018

DOI: 10.1021/acsnano.7b08418
ACS Nano 2018, 12, 2569–2579

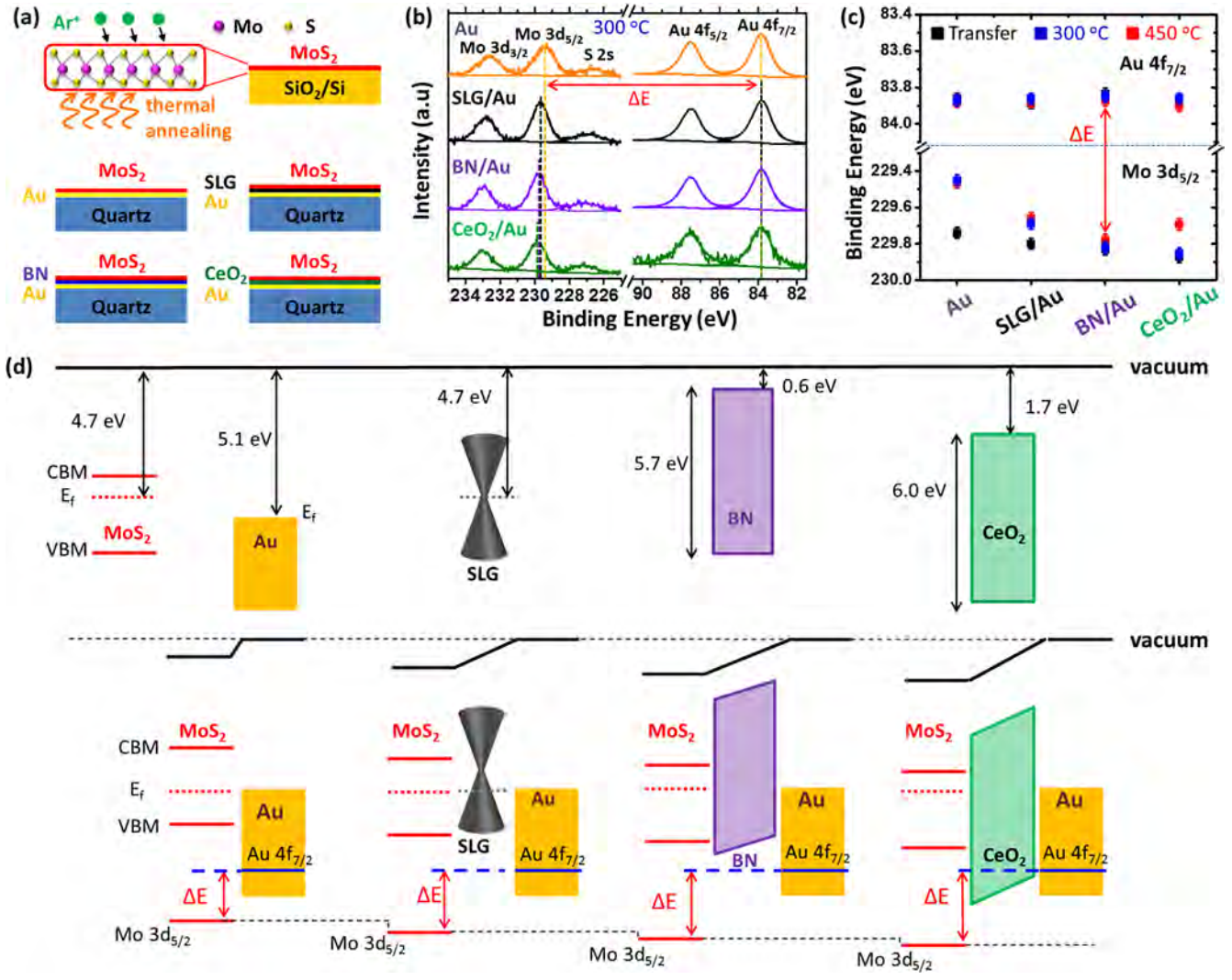

Figure 1. Illustration of MoS_2 on various substrates, X-ray photoelectron spectra, and band structure. (a) Four structures studied in this work: MoS_2/Au, MoS_2/SLG/Au, MoS_2/BN/Au, and MoS_2/CeO_2/Au. All the structures are supported by quartz substrates. The MoS_2 single layers in all these structures were transferred from CVD grown MoS_2 on Si/SiO_2 substrate. Vacuum thermal annealing or Ar^+ irradiation was used to treat the samples to enhance either the contact with substrates or produce defects. (b) XPS at the Mo 3d and Au 4f peaks of MoS_2 on the four substrates: Au, SLG/Au, BN/Au, and CeO_2/Au. All samples were measured after vacuum annealing at 300 °C under 10^{-9} mbar. The dashed vertical lines illustrate the binding energies of Mo $3d_{5/2}$ and Au $4f_{7/2}$ electrons. (c) Binding energies of the Mo $3d_{5/2}$ and Au $4f_{7/2}$ for the four samples after transfer and vacuum annealing at 300 °C and 450 °C. The red arrow illustrates ΔE, the binding energy difference between the Au $4f_{7/2}$ and Mo $3d_{5/2}$ photoemission peaks. (d) Illustration of the energy band alignment for the four samples. The upper four graphs show the materials before contact, and the lower four show the state after contact between MoS_2 and the substrates and the shift of MoS_2 energy level due to the interaction between MoS_2 and substrate. Vacuum level, valence band maximum (VBM), conduction band minimum (CBM) of MoS_2, Fermi levels (E_f) of MoS_2 and Au are labeled.

netic,[13] and optical[14] properties of MoS_2. For example, in electrochemical applications, recent experiments and theories[10,11,15] show that S-vacancies in the basal plane of MoS_2 can activate the catalytic reactivity of MoS_2. By introducing S-vacancies and suitable strains in SL MoS_2, Li *et al.*[11] achieved the highest activity so far for the hydrogen evolution reaction (HER). In terms of electronic properties, on the other hand, defects such as vacancies, dislocations, and grain boundaries reduce the electronic mobility in MoS_2 prepared using chemical vapor deposition (CVD), by several magnitudes compared to MoS_2 exfoliated from single-crystal bulk.[12] Regarding optical properties, Tongay *et al.*[14] experimentally demonstrated that S-vacancies induce new photoluminescence (PL) peaks and enhance the PL intensities. In magnetics, Han *et al.*[13] reported ferromagnetic effects resulting from anion and cation vacancies and vacancy clusters in MoS_2.

Although the role of MoS_2 defects in altering the properties has been widely recognized, there are still open questions at a deeper and mechanistic level for connecting the presence and type of defects to electronic, optical, and catalytic characteristics. For example, only S-vacancies were considered in activating the MoS_2 basal plane to enable the HER, while other types of defects, such as Mo-vacancies, have not been studied in detail.[10,11] Moreover, CVD MoS_2 shows n-type electronic conductivity.[16] Qiu *et al.*[17] and Ugeda *et al.*[18] believed that this phenomenon is caused by the S-vacancies and by the resulting defect donor states in MoS_2. However, Komsa *et al.*[19] found that through first-principles calculations, the S-vacancies form acceptor states rather than donor states in the

DOI: 10.1021/acsnano.7b08418
ACS Nano 2018, 12, 2569−2579

MoS_2 energy bands. Therefore, the n-type conductivity in CVD MoS_2 remains elusive despite the fact that S-vacancies are the most common defects in MoS_2 prepared by the CVD process. Recently, Yu *et al.*[20] proposed that the donor states in polycrystalline MoS_2 stem from defect complexes made of a dislocation and two S-vacancies.

To understand the role of defects in MoS_2 functionality, in this work, we systematically assessed the impact of defects on the electronic structure of SL MoS_2 model system on several different substrates. The SL MoS_2 used in our study was prepared through CVD synthesis.[21] The substrate layers used beneath the MoS_2 layer were Au, SL boron nitride (BN)/Au, SL graphene (SLG)/Au, and CeO_2/Au. Methods commonly used to create defects in MoS_2 in literature included vacuum thermal annealing,[14,17,22] electron irradiation,[9,12] plasma treatment,[10] Se insertion,[23] and ion irradiation.[14,24−30] In this work, we introduce lattice defects in SL MoS_2 by both thermal annealing in vacuum and by Ar^+ ion irradiation. While both approaches to create defects in MoS_2 have been used in previous literature as noted above, here we reveal the electronic structure induced by lattice defects formed in those ways. This information helps to interpret the mechanisms by which the defects alter the properties of MoS_2. The presence of defects in MoS_2 was confirmed by X-ray photoelectron spectroscopy (XPS) as well as Raman and PL spectroscopies. Both XPS and scanning tunneling microscopy/spectroscopy (STM/STS) showed that the defects in the MoS_2 can change the electronic energy levels in MoS_2 and introduce defect states in the bandgap. Raman and PL spectroscopies can be sensitive and convenient tools to probe the defects in MoS_2. The presence of defect states within the bandgap was observed using STS, which is likely to be associated with S-vacancies and Mo-vacancies, and matches well with our molecular dynamics (MD) and density functional theory (DFT) simulations. In addition, the reduction in the oxide substrate (CeO_2) was also found to change the band alignment between MoS_2 and the substrate. This finding demonstrates that MoS_2 electronic structure is tunable by controlling the defect and charge-transfer states of the underlying red-ox active oxide substrate. We also demonstrated that the introduction of defects by ion irradiation can effectively enhance the HER activity. As a result, our work provides a detailed electronic structure description of defected MoS_2 on various substrates and demonstrates that introducing defects can be effective in improving the functionality of 2D materials.

RESULTS AND DISCUSSION

Single-layer MoS_2 forms a hexagonal lattice structure from the top view and has three sublayers of atoms, one layer of Mo atoms sandwiched between two layers of S atoms (Figure 1a).[4,5] Figure 1a also shows the structures studied in this work and the processes of thermal annealing and ion sputtering. First, we look at the impact of thermal annealing on the electronic structure of SL MoS_2 on various substrates. XPS measurements were performed on the MoS_2 samples on different substrates after transfer and after annealing at 300 °C and 450 °C under 10^{-10} mbar base pressure. Figure S1f shows a representative XPS survey spectrum of SL MoS_2 on Au/quartz substrate. The optical microscope images of all the samples, as well as the atomic structure of MoS_2, are shown in Figure S1. Peaks of all the elements can be easily observed and are labeled, including Mo 3p, Au 4d, C 1s, Mo 3d, S 2p, and Au 4f. We mainly study the Mo $3d_{5/2}$ peak position relative to the Au $4f_{7/2}$ peak. A change in this relative position is indicative to charge transfer between MoS_2 and Au (Figure 1b). We define ΔE as the binding energy difference between the Au $4f_{7/2}$ and Mo $3d_{5/2}$ photoemission peaks (labeled in Figure 1b,c). We use changes in ΔE as a measure of the energy level shifts in MoS_2.

For MoS_2 transferred on to different substrates, the Au $4f_{7/2}$ has almost no variation in binding energy (Figure 1b,c). In contrast, Mo $3d_{5/2}$ has different binding energies depending on the substrate, as seen in Figure 1c. The Mo $3d_{5/2}$ peak is at 229.74 eV for MoS_2/Au after transfer (prior to annealing), but shifted to higher binding energies by 0.06, 0.08, and 0.13 eV for MoS_2/SLG/Au, MoS_2/BN/Au, and MoS_2/CeO_2/Au, respectively, as shown with black squares in Figure 1c. The different binding energy of Mo $3d_{5/2}$ electrons is attributed to the different band alignments between MoS_2 and the substrates. The mechanism of this phenomenon is illustrated in Figure 1d. The basic assumption is that when MoS_2 in contact with the substrate, there will be a potential energy change that lifts up or shifts down the MoS_2 energy level (Figure 1(d)), as demonstrated in refs 34 and 37. Au has an electron affinity of 5.1 eV, larger than MoS_2 (4.7 eV).[31−33] Since Au substrate is a metal and has an abundance of electrons, the Fermi level of the semiconducting MoS_2 needs to be aligned with the Fermi level of Au. When MoS_2 is directly in contact with Au, electrons transfer from MoS_2 to Au substrate, leading to a downshift of MoS_2 Fermi level position within the bandgap. It is important to recall that an interface charge or interface dipole can be formed between MoS_2 and Au which is due to the interaction of MoS_2 and Au and the creation interfacial state.[34] Such interface charge can cause a small potential drop across the MoS_2 and Au interface, as shown in Figure 1d. When there is a layer of graphene inserted between MoS_2 and Au, electrons from both the MoS_2 layer and graphene will transfer to Au. Interface dipoles were reported to exist in MoS_2/graphene[35] and graphene/Au interfaces,[36] which lead to a larger potential in MoS_2/SLG/Au compared to MoS_2/Au, as shown in Figure 1d. Accompanied with the creation of a larger potential drop across the interface by inserting SLG (Figure 1d), the binding energy of Mo $3d_{5/2}$ electrons in MoS_2 increases, resulting in a larger ΔE in MoS_2/SLG/Au compared to MoS_2/Au. Due to the insulating nature of hBN and CeO_2 layers, charge can be accumulated on both sides of the BN and CeO_2 interface, thus contributing to a large potential drop across the middle layer, leading to a down shift of MoS_2 energy level and the alignment of Fermi levels of MoS_2 and Au (Figure 1d). As a result of this down shift of energy level, the Mo $3d_{5/2}$ binding energy at the MoS_2 surface is further increased by adding a BN and CeO_2 layer. These results indicate that SLG, BN, and CeO_2 can be effective media to partially screen interface charge transfer directly from MoS_2 to Au, which is ubiquitous at the interface of MoS_2 and many metals.[34] Therefore, these substrates can facilitate the applications of electronic devices based on MoS_2. It is important to note that the energy shifts of the valence band, conduction band, and core level due to the interface potential drop are not necessarily the same quantitatively. The actual quantitative changes in each energy level depend on the details of how the band structure evolve upon charge transfer at the interface.[34,37] Our explanation is qualitative and only shows the trend of how the energy level changes for different samples.

Annealing at 300 °C in vacuum increases the variation of ΔE (Figure 1b,c) among the different substrates. As can be seen by data (blue squares) in Figure 1c, upon annealing at 300 °C and compared to the as-transferred states, Mo $3d_{5/2}$ shifts to even

DOI: 10.1021/acsnano.7b08418
ACS Nano 2018, 12, 2569−2579

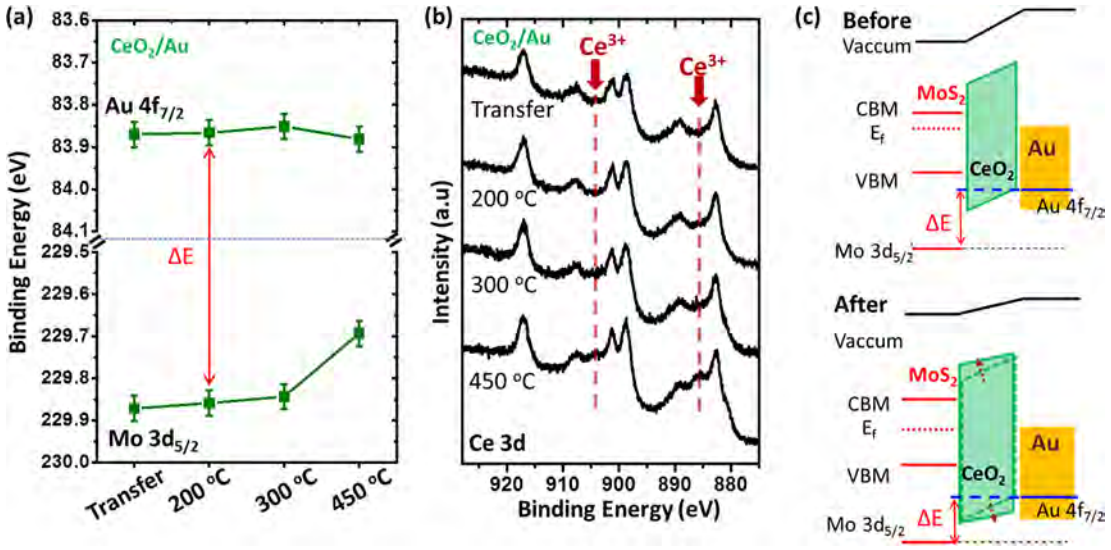

Figure 2. Shift of the Mo $3d_{5/2}$ binding energy and Ce^{4+} reduction to Ce^{3+} during annealing. (a) The binding energies of the Mo $3d_{5/2}$ and Au $4f_{7/2}$ electrons for the $MoS_2/CeO_2/Au$ sample after transfer and after annealing at 200 °C, 300 °C, and 450 °C. (b) The Ce 3d X-ray photoelectron spectra of $MoS_2/CeO_2/Au$ samples after each annealing step. The dashed red lines indicate the appearance of Ce^{3+} peaks after 450 °C annealing. (c) Illustration of energy band alignment for the $MoS_2/CeO_2/Au$ sample. The upper graph shows the bands before the Ce^{4+} reduction, and the lower one shows the bands after the Ce^{4+} reduction.

lower binding energies on MoS_2/Au and MoS_2/SLG/Au, while the Mo $3d_{5/2}$ remains almost unchanged on MoS_2/BN/Au and MoS_2/CeO_2/Au. The binding energy of Au $4f_{7/2}$ remains the same after thermal annealing. The removal of water or gas residues between MoS_2 and the substrates and a better contact between MoS_2 and the substrates[38] after annealing at 300 °C are a likely reason for these changes. Hence the charge-transfer process between MoS_2 and Au or between MoS_2 and SLG/Au was enhanced by thermal annealing, resulting in a smaller potential drop across the interface and a smaller ΔE values.

Next, we show further evidence to the charge transfer between MoS_2 and different substrates based on the Raman and PL spectra measured after annealing at 300 °C. Figure S2a shows the Raman modes of all the samples, including the E′ (around 385 cm^{-1}) and A_1' (around 405 cm^{-1}) modes. All spectra are normalized by the intensity of the A_1' mode. Note that the notations E′ and A_1' are for SL MoS_2 with D_{3h} symmetry, and they become E_{2g} and A_{1g}, respectively, for bulk MoS_2 that has D_{6h} symmetry.[39] Clearly, the A_1' peak is red-shifted after transfer, and all substrates induce peak widening compared to the as-grown sample. Since A_1' is sensitive to doping,[40] it is reasonable to infer that the substrates introduce p-type doping to MoS_2, which is also consistent with our XPS results and with the literature.[41] The E′ peaks also widen and redshift after transfer, which indicates the strain introduced during the transfer process.[7,42] The corresponding PL spectra shown in Figure S2b, which are also normalized by the A_1' peaks, suggest the presence of strain and doping effects in MoS_2 as well. As can be seen, the as-grown sample shows z strong and narrow PL peak at around 1.85 eV. The suppression of the PL peaks of MoS_2 on Au and SLG/Au substrates is due to the metallic nature of the substrates and the subsequent charge transfer that occurs between MoS_2 and the substrate and the PL quenching effect. We can still observe a very weak PL peak for MoS_2/SLG/Au, which suggests the charge-transfer effect in MoS_2/SLG/Au is not as strong as in MoS_2/Au. This is in line with our XPS results in Figure 1b,c that the binding energy of Mo $3d_{5/2}$ is slightly higher for MoS_2/SLG/Au than for MoS_2/Au. The PL peaks for MoS_2/BN/Au and MoS_2/CeO_2/Au are still strong, indicating the insulating nature of these two substrates, again consistent with the findings from XPS in Figure 1b,c. However, the PL peaks are widened compared to as-synthesized MoS_2, which is likely due to the transfer process.

The effect of annealing to a higher temperature, 450 °C is also shown in Figure 1b,c. For MoS_2 on Au, SLG/Au, and BN/Au, the Mo $3d_{5/2}$ binding energy does not show much difference between 300 °C and 450 °C. However, the CeO_2/Au substrate induces a considerable decrease of ΔE by about 0.18 eV after annealing at 450 °C. Figure 2a also confirms that Au $4f_{7/2}$ binding energy is not affected either by the thermal annealing or by the reduction of CeO_2. In fact, as observed in Figure 2a, the binding energy of Mo $3d_{5/2}$ remains at about 229.85 eV for an as-prepared sample as well as after annealing at 200 and 300 °C. After annealing at 450 °C, however, the binding energy of Mo 3d decreases to about 229.7 eV. It is important to recall here that CeO_2 is a red-ox active material and loses oxygen upon annealing in reducing conditions;[43−47] that is, annealing in ultrahigh vacuum (UHV) as in this experiment. A 450 °C is high enough temperature to enable oxygen mobility and therefore enables reduction of CeO_2 to a reduced, oxygen-deficient state. It is clear in the X-ray photoelectron spectra of Ce 3d electrons in Figure 2b that the Ce^{3+} peaks at binding energies of 886 and 904 eV are enhanced after 450 °C, confirming that Ce^{4+} in CeO_2 is partially reduced to Ce^{3+}. Reduced CeO_{2-x} is a mixed ionic electronic conductor, and electronic conduction ocurrs through hopping of localized Ce 4f electrons from Ce^{3+} to Ce^{3+} sites.[48,49] Because of electronic conductivity of reduced CeO_{2-x}, a smaller potential drop takes place in the CeO_2 layer of the $MoS_2/CeO_2/Au$ structure compared to its fully oxidized state and therefore a smaller shift of energy level in MoS_2. Consequently, a smaller binding energy of Mo $3d_{5/2}$ and a smaller ΔE prevail, as shown in Figure 2c.

Thermal annealing itself did not introduce any noticeable defects into MoS_2. Upon annealing in UHV to 450 °C, our XPS results showed that the Mo 3d peak shapes did not change

DOI: 10.1021/acsnano.7b08418
ACS Nano 2018, 12, 2569−2579

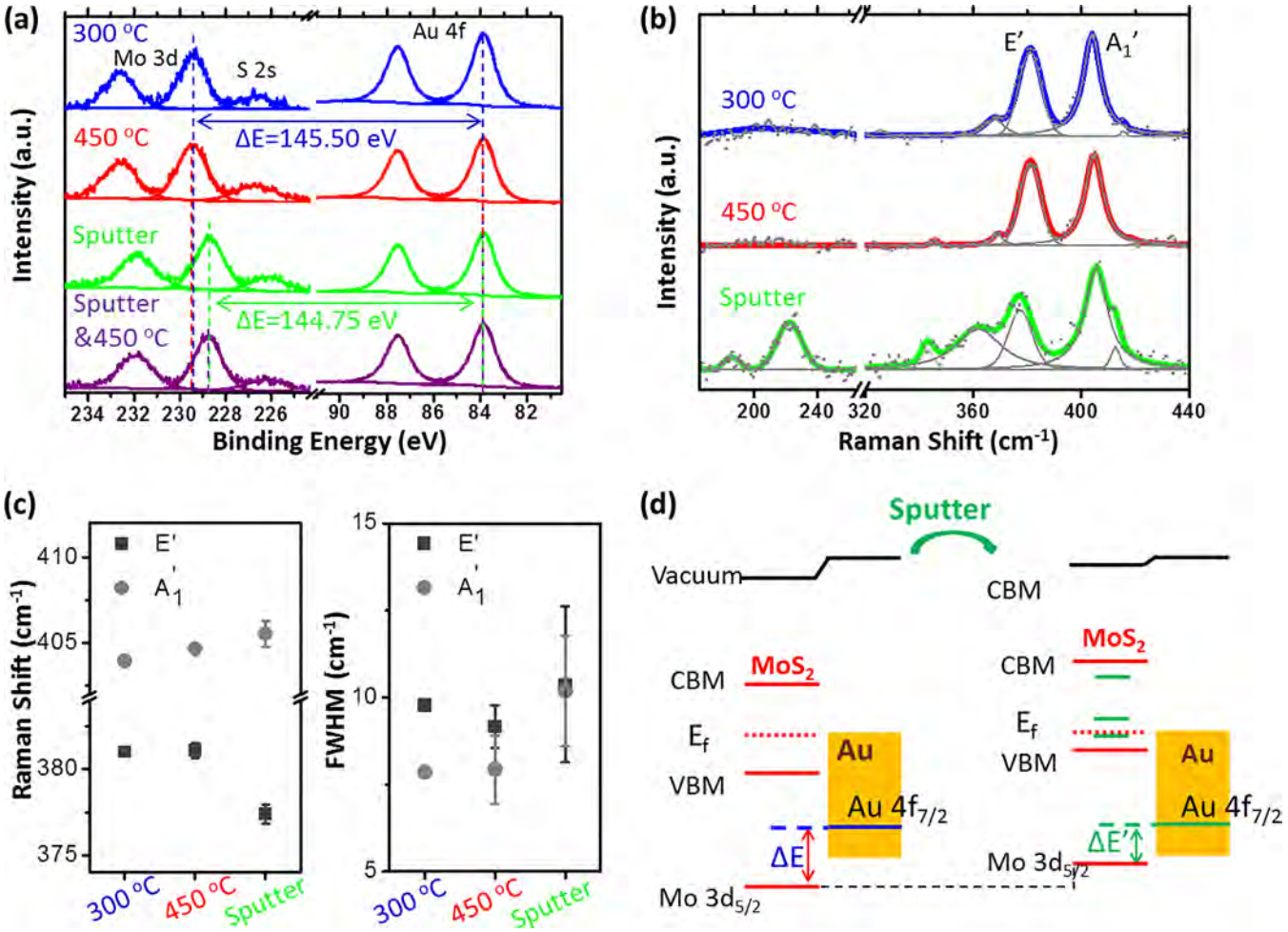

Figure 3. XPS and Raman characterization of samples before and after introducing defects by Ar^+ sputtering for MoS_2 on Au substrate. (a) X-ray photoelectron spectra of the Mo 3d, S 2s, and Au 4f electrons in the MoS_2/Au sample after annealing at 300 °C and 450 °C in UHV, sputtering, and sputtering with subsequent annealing at 450 °C. Δ*E* for the upper two and the lower two plots are shown. (b) Raman spectra of the MoS_2/Au sample after annealing at 300 °C and 450 °C in UHV and after sputtering. The MoS_2 Raman peaks E′ and A_1′ are labeled. All spectra are normalized by the corresponding A_1′ peaks. The measured data are shown as dots. Fitted individual peaks and overall spectra are shown as gray and colored curves, respectively. (c) Raman shift and fwhm of E′ and A_1′ peaks for the MoS_2/Au sample after annealing at 300 °C and 450 °C and after sputtering. (d) Illustration of energy band alignment for the MoS_2/Au sample. The left graph shows the bands before sputtering, and the right one shows the bands after sputtering.

(Figure 3a). The intensity ratio of the Mo and S photoemission peaks did not change after annealing at 450 °C (Figure S3b). These mean that MoS_2 remained stable and without detectable formation of defects upon annealing alone. This is consistent with Raman results presented later in the paper (Figure 3b,c). However, thermal annealing changed the coupling between MoS_2 and the substrate by improving the contact between MoS_2 and the substrate[38] in MoS_2/Au, MoS_2/SLG/Au, and MoS_2/BN/Au or by introducing defects into the reducible substrate CeO_2 in MoS_2/CeO_2/Au. Both effects significantly change the band alignment between MoS_2 and the substrate and can have a significant impact on the device performance, since many electronic and optoelectronic devices depend on the energy levels and band alignment of MoS_2.[38]

As stated in the Introduction, ion irradiation is another way to create defects and defect-induced electronic states in 2D materials. Heavy ion irradiation is shown to introduce extended defects such as incisions and folds in 2D materials including MoS_2.[50] Here we focus on lattice defects that can be created by low-energy ion irradiation. We introduced lattice defects into SL MoS_2 by low-energy Ar^+ sputtering and studied the change of photoemission binding energy, peak shape, and optical properties for MoS_2 on Au substrates. As shown in Figure 3a, the defects introduced by ion irradiation did significantly alter the band alignment between MoS_2 and Au. The Mo $3d_{5/2}$ binding energy decreased by 0.8 eV, and the Au $4f_{7/2}$ peak remained unchanged after sputtering with 0.5 keV Ar^+ ion beam for 1 min. In contrast to this significant energy shift upon sputtering, no change in Δ*E* was detectable between annealing at 300 °C and 450 °C. Re-annealing the sputtered samples at 450 °C does not change the band alignment further.

To provide more quantitative information about the defects in MoS_2 after sputtering, we performed Raman and PL spectra measurements on the MoS_2/Au samples before and after sputtering. Figure 3b shows the Raman spectra of MoS_2/Au after 300 °C and 450 °C annealing and sputtering. The E′ and A_1′ modes of MoS_2 are easily observed, and all spectra are normalized by A_1′ modes. As can be seen, Raman spectra do not show considerable differences for 300 °C and 450 °C annealing, but after sputtering, E′/A_1′ modes are red/blue-shifted, and both are widened (Figure 3c). There is a shoulder (at around 362 cm^{-1}) on the left of E′ mode and one (at

DOI: 10.1021/acsnano.7b08418
ACS Nano 2018, 12, 2569−2579

around 415 cm^{-1}) to the right of A_1' mode, which are assigned as defect modes,[28] but without a clear identification of the defect type. Both peaks are significantly enhanced after sputtering, another feature confirming the introduction of defects with sputtering. At about 220 cm^{-1}, there is an LA mode which also indicates the existence of defects for MoS_2, and this mode becomes considerable after sputtering.[28] The corresponding PL peaks (Figure S3c) show that after sputtering, PL peaks totally disappear. PL in MoS_2 is generated due to the radiative decay of excitons which binds electrons and holes near the edges of conduction and valence bands.[5,51] The reduction of the PL peak intensities indicates that the electronic structure changed due to a large defect density, and the population of the defect states increases the nonradiative decay channel of excitons.

The evolution of Raman peaks with thermal annealing and sputtering is summarized in Figure 4c. There is an obvious red

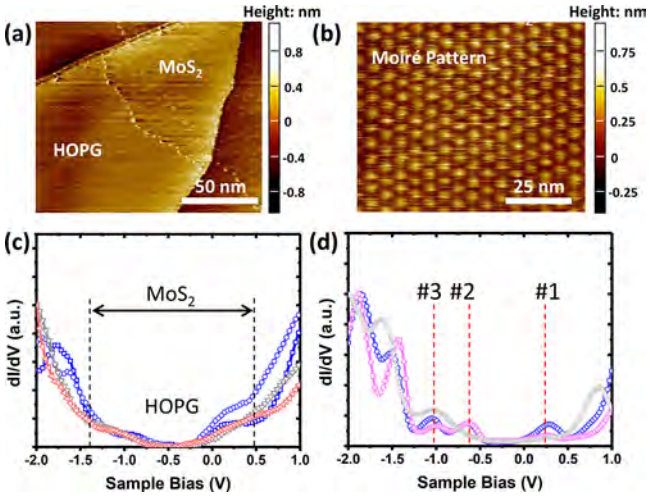

Figure 4. STM image and dI/dV on MoS_2 with and without defects on HOPG substrate. (a) STM constant current image of MoS_2 on HOPG, and the Moiré pattern between MoS_2 and HOPG hexagonal lattices can be observed. Imaging conditions: I_{tun} = 50 pA, V_{sample} = −1.5 V. (b) Zoom-in on the MoS_2 zone in the STM image in (a). (c) dI/dV spectrum on the MoS_2 on HOPG prior to ion irradiation. A lock-in preamplifier was used with 30 mV at 1 kHz frequency. The Dirac cone of graphite and the MoS_2 band gap can be observed. The four dI/dV curves were measured at different locations on the sample. (d) dI/dV spectrum of MoS_2 on HOPG after being ion irradiated with 500 eV Ar^+. Three clear defect states can be observed. The curves were measured at different locations on the sample.

shift in E′ peak and blue shift in A_1' peak after sputtering. Both peaks are widened as well, and the variation for the peaks also increases after sputtering. As reported before,[28] defects in MoS_2 can cause the frequency shifts and widenings in E′ and A_1' peaks observed here. From the Raman signatures, we can also deduce interdefect distances to be 1.60 ± 0.03 nm (defect density 7.46 ± 0.42 × 10^{12} cm^{-2}) after sputtering.[28] Thus, our Raman measurement manifests itself as a sensitive and nondestructive approach to probe the defects in MoS_2, which is in good agreement with the XPS measurements. The introduction of defect states in MoS_2 is illustrated with green levels within the gap in Figure 3d. The reason for the change of band alignment between MoS_2 and Au as observed in XPS measurement (Figure 3a) is likely due to the creation of defect states within the band gap of MoS_2, which greatly facilitates the charge-transfer process between MoS_2 and Au. Hence, a decrease of interface potential drop and a smaller ΔE (Figure 3d) were observed. More detailed information on defect-related states in the gap will be discussed in STM/STS Measurements section later.

Besides MoS_2/Au, we also observed similar Raman and PL changes on other samples after sputtering. For example, Figure S4 shows the Raman and PL spectra of MoS_2/BN/Au sample after 300 °C and 450 °C annealing and after sputtering. Similar defect-related Raman modes (the 362 cm^{-1} mode and the LA mode at 220 cm^{-1}) appear after sputtering, E′ and A_1' peaks widen after sputtering, and they red and blue shift, respectively, all indicating the introduction of defects (Figure S4c,d). The PL peak for MoS_2/BN/Au disappears after sputtering, indicating the introduction of in-gap defect states and the change of energy band structure (Figure S4b).

As shown above, the XPS and Raman spectroscopy indicate formation of defect states within the bandgap of MoS_2, leading to a stronger charge transfer between MoS_2 and Au substrate. To provide more direct information on the electronic structure of ion irradiated MoS_2, we performed scanning tunneling microscopy (STM) and tunneling spectroscopy (dI/dV spectroscopy) on SL MoS_2 in its as-transferred state and after introducing defects by Ar^+ sputtering. We transferred pristine MoS_2 onto highly oriented pyrolytic graphite (HOPG) substrates using a water-assisted method, leaving a clean and residue-free surface of MoS_2. The boundary between HOPG substrate and SL MoS_2 can be seen clearly in Figure 4a, with the Moiré pattern of MoS_2 and HOPG lattices in MoS_2/HOPG region shown in Figure 4b. The presence of the Moiré pattern indicates a coherent interface between MoS_2 and HOPG substrate. The dI/dV spectra, representing the density of states (DOS), on MoS_2 on HOPG prior to irradiation is in Figure 4c. The dI/dV shows both the Dirac cone of graphite and the edges of the conduction band and valence band of MoS_2. The HOPG substrate contributes to the dI/dV spectra, and hence it was difficult to precisely quantify the MoS_2 bandgap. Based on the slope change in the spectra, we approximate the bandgap to be 1.9 eV, a slightly smaller value than other works reported for pristine monolayer MoS_2.[52−55] The MoS_2 layers were sputtered with 500 eV Ar^+ ions for 1 min in the STM chamber, the same procedure as the other samples presented in Figure 3. Sputtering led to poor image resolution, and therefore it was not possible to obtain tunneling spectra precisely on individual atomic defects. We collected spectra on various locations to obtain a general result on the defected surface. The dI/dV spectra shown in Figure 4d are representative spectra that show defect states after ion irradiation. Three new peaks in the bandgap located approximately 0.3 eV (#1), 1.2 eV (#2), and 1.6 eV (#3) below the conduction band minimum can be observed (Figure 4d). Previous work has reported the STS of bulk MoS_2 which shows in-gap defect states as well.[56] Since the defect density in our sample is large, as quantified from Raman to be close to 10^{12} cm^{-2}, we may see defect states from several defect types and configurations in the dI/dV spectra. These results qualitatively indicate the existence of different types of defects located at different energy positions. This is a reasonable outcome given the nature of ion irradiation induced defects. As will be shown by theoretical calculations later, the peaks closer to valence band (#2, #3) are likely related to the Mo-vacancies, and the one closer to the conduction band (#1) may arise from single or double S-vacancies.[11] Calculations of

DOI: 10.1021/acsnano.7b08418
ACS Nano 2018, 12, 2569−2579

defect states arising from different type of defects as described below support this interpretation. The variation of dI/dV taken at different locations at the surface is also shown in Figure S5.

To identify the likely type of defects upon irradiation of MoS_2 and to associate those defects with the electronic states shown in Figure 4d, MD simulations and first-principles calculations, respectively, were carried out. In MD simulations, Ar^+ ion with incident energy of 500 eV was initially placed at 20 Å above the freestanding SL MoS_2 sheet, and the incident direction is perpendicular to the MoS_2 sheet (Figure 5a). The

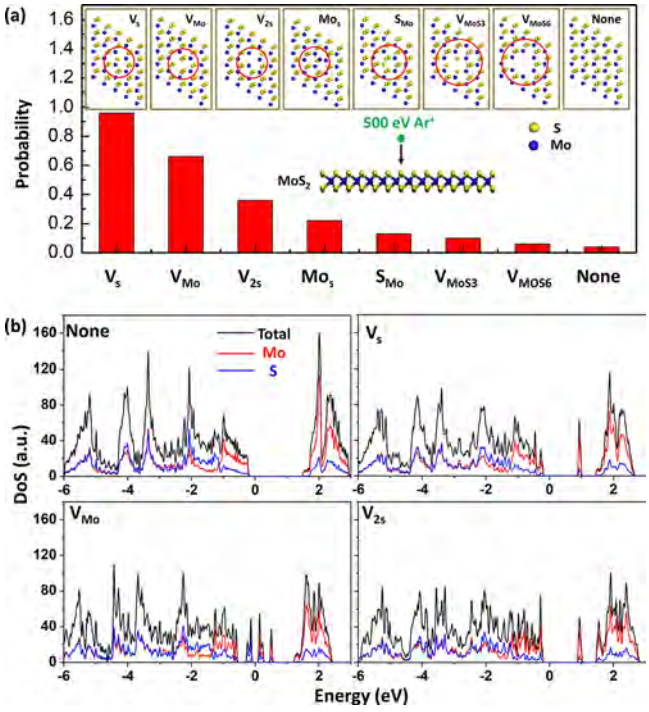

Figure 5. Possible defect structures that can be introduced by sputtering and the local electronic structure changes caused by these defects. (a) The probability density for different defect structures to form after 500 eV Ar^+ sputtering, as found from MD simulations. (b) The total DOS and the contributions from the Mo and S states in MoS_2 with no defects and with three types of defects, V_s, V_{2s}, and V_{Mo}.

most likely defect configurations upon ion irradiation in MoS_2 were found as single S-vacancy (V_s), single Mo-vacancy (V_{Mo}), double S-vacancy (V_{2s}), S replaced by Mo (Mo_S), Mo replaced by S (S_{Mo}), Mo and three S-vacancy (V_{Mo3s}), and Mo and six S vacancy (V_{Mo6s}) (Figure 5a). Figure 5b presents the DOS as a function of energy for SL MoS_2 without defects, and the DOS with V_s, V_{Mo}, V_{2s} (the three most probable defects) as determined by DFT calculations. From Figure 5b, S-vacancies introduce defect states within the energy gap close to the bottom of the conduction band, while the less probable Mo-vacancy is more likely to introduce defect states closer to the top of the valence band.[12] This result is consistent with previous reports.[12,57,58] Using STEM, Zhou *et al.* observed single-vacancy, double S-vacancy, and vacancy complex of Mo as intrinsic defects in SL MoS_2. They reported that S-vacancies caused defects state within the band gap that is closer to conduction band, while the vacancy complex of Mo lead to states that are closer to valence band.[12] Tongay[53] reported S vacancy formation in SL MoS_2 after He^+ irradiation, which introduced defect states near the conduction band. Comparing the electronic structure of defected MoS_2 probed by dI/dV (Figure 4d) with the DFT results, we infer that the S-vacancies (both single and double S-vacancies) and single Mo-vacancies dominate the changes in the electronic structure resulting from Ar^+ sputtering observed in both XPS and dI/dV.

It is worth noting that we cannot rule out the contribution from other defect configurations, such as Mo_S, S_{Mo}. However, their presence is expected to be less than the three major defects examined in Figure 5b. The electronic structures of SL MoS_2 with these defect configurations are shown in Figure S6. Some of these defects states have signatures in DOS as V_s, V_{2s}, and V_{Mo}. As can be seen from Figure 5 and Figure S6, the main defects we observed in MD simulation are vacancies for the irradiation conditions we used. Interstitials are barely observed. This is because interstitials are very unstable. Due to the small migration energy of interstitials, they tend to migrate to other sites and form stable and regular defect forms. Figure S7 shows a representative relaxation process of S interstitial formed by Ar^+ sputtering. The formation of vacancies is mainly balanced by sputtered ions. As shown in Figure S7c, the number of sputtered atoms as a function of Ar^+ sputtering energy reached a peak at 500−600 eV. In previous works, thermal annealing at 500 °C is considered to mainly cause S-vacancies in MoS_2.[57] Here we report that with ion sputtering introduces other types of defects because of atom sputtering and mixing effects. Hence ion sputtering provides a potential way to tune the defect states of MoS_2 and other 2D materials, beyond thermal annealing and thermodynamic defect equilibria. Furthermore, as expected, our MD simulation results demonstrate the possibility of forming different defect configurations by varying the ion energy, as shown in Figure S8 for 200, 500, and 2000 eV Ar+ ion sputtering. By selecting the appropriate ion sputtering conditions, it is possible to tune the properties and performance of 2D functional materials.

Finally, as one demonstration of tuning the functionality of MoS_2 through defect engineering, we test the HER activity of the as-synthesized MoS_2 single layer and the one with defects introduced by ion sputtering. We use an inert substrate, glassy carbon, for this experiment. As shown in Figure 6a, the pristine MoS_2 transferred on glassy carbon shows strong E′ and A_1′ Raman peaks with no defect peaks at 362 or 220 cm^{-1}. After

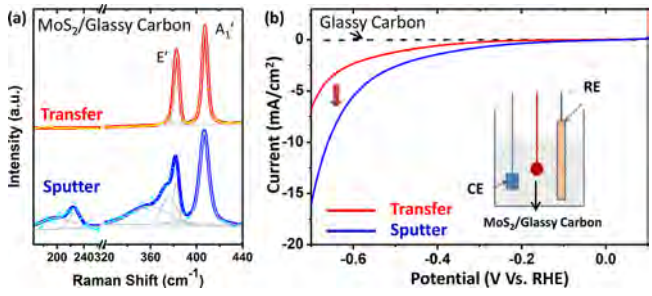

Figure 6. Raman characterization and HER measurement of MoS_2 on glassy carbon. (a) Raman spectra of the sample without sputtering (top spectrum) and after 2 min 0.5 keV Ar^+ sputtering (bottom spectrum). The dots are measured data, and the solid curves are fitted peaks and spectra. The peaks at around 220 and 362 cm^{-1} indicate defects. The spectra are normalized by the corresponding A_1′ modes. (b) Linear sweep voltammetry curves for glassy carbon substrate and for MoS_2 on glassy carbon before and after sputtering with Ar^+ ions. The inset figure shows the HER measurement set up.

DOI: 10.1021/acsnano.7b08418
ACS Nano 2018, 12, 2569−2579

500 eV Ar^+ ions sputtering MoS_2 for 2 min, the sample shows distinct defect peaks, and the intensities of E′ and A_1′ peaks are decreased, consistent with Figure 3b. The HER reaction kinetics is faster, with a higher current density on MoS_2 that was ion sputtered (Figure 6b). This result clearly demonstrates the enhancement of HER kinetics after introduction of defects, because of activating the inert basal plane of MoS_2 for HER by creating S vacancies[11,59] upon Ar^+ irradiation. Results indicate a good potential for the application of defect engineering of MoS_2 and other TMD materials.

In addition to hydrogen evolution and catalytic devices, the defect and interface engineering of MoS_2 can also be applied in electronic and photonic devices. For example, the band alignment of MoS_2 and the substrate may create interfacial regions for effective light harvesting or generation.[60−62] The substrates are known to affect also the PL properties of MoS_2, inducing tunable light-emitting features.[60] Since defects influence the light emitting, electron mobility, and ferromagnetic properties of MoS_2, customized electronic and photonic devices with targeted defects can be fabricated. For example, as indicated by previous studies, stronger PL was observed by introducing defects in MoS_2, which may inspire MoS_2-based photonic devices.[14] Meanwhile, as defects and substrates alter the band structure of MoS_2, targeted selection of substrates can help engineer various electronic devices that can be designed and engineered, such as tunneling field-effect transistors.[63,64] In addition, using oxide substrates such as CeO_2 in this work, electronic and photonic devices tunable by temperature can potentially be fabricated and operated.

CONCLUSION

In conclusion, we performed a systematic study of the effects of substrate and defects on SL MoS_2 electronic structure using XPS, Raman and PL spectroscopies, and STM/STS. Thermal annealing in UHV considerably improved the contact between MoS_2 and substrate, facilitating charge transfer between MoS_2 and metallic substrates like Au and SLG/Au and causing energy band shift in MoS_2. In addition, and importantly, reduction of the CeO_2 substrate upon annealing significantly affects the energy band alignment of MoS_2 and CeO_2/Au substrate, because the reduction introduces electronic conductivity into this substrate. Defects introduced by ion sputtering influenced the electronic structure of MoS_2 and band alignment of MoS_2/Au heterostructure. The local defect states within the band gap were identified by STM and dI/dV spectra. The MD and DFT simulations indicate that these defect states are likely to be single and double S vacancies and single Mo vacancies. In addition, we demonstrated that the introduction of defects by ion sputtering enhances HER activity of SL MoS_2. Tunability of defect types and concentrations in MoS_2 by ion sputtering at different energies provides a possibility to engineer the properties of MoS_2 as well as other 2D materials. This work demonstrates an effective set of spectroscopic methods, supported by atomistic and electronic calculations, to probe the band shift, charge transfer, and defect states in MoS_2, which are sensitive to substrate, thermal annealing and ion sputtering. Our results show the importance and potential of defect engineering in tuning the functionality of MoS_2 and other TMD materials in electronics, optoelectronics, and electrochemistry.

METHODS

CVD Synthesis of Monolayer MoS_2. Monolayer MoS_2 films were grown on SiO_2/Si substrates by atmospheric pressure CVD.[21] Prior to the growth, the substrates were etched in KOH solution for 5 min to make them hydrophilic and rinsed with deionized (DI) water. Then, perylene-3,4,9,10-tetracarboxylic acid tetrapotassium salt (PTAS) was spin coated on substrate for different samples. The sulfur precursor (15−33 mg) was loaded in an alumina boat and placed at 14 cm from the furnace center. MoO_3 powder (18−20 mg) was added to a second alumina boat, of which the PTAS-coated substrates were placed on top of the alumina boat facing down. The second boat was loaded into the center of the furnace for growth. The growth process was performed in a tube furnace at a sample temperature of 650 °C. The growth was carried out for 3 min, during which argon (5 sccm) was used as a carrier gas. An argon flow rate of 1000 sccm was used before the growth to purge the tube and after the growth to quench the growth process.

MoS_2 Transfer. To transfer MoS_2 from a Si/SiO_2 substrate to another substrate, PMMA was first spin-coated on MoS_2 on the Si/SiO_2 substrate. After baking at 80 °C, the chip was put in KOH solution, which etched away the SiO_2 layer. After rinsing in DI water, the MoS_2-PMMA film was transferred onto the target substrate, followed by soaking in acetone to remove the PMMA layer. The procedures to transfer monolayer graphene or BN were generally the same as for MoS_2, except that $FeCl_3$ was used to etch the Cu substrate for CVD grown graphene and BN. The detailed growth procedure for monolayer BN and graphene can be found in previous reports.[65−67] The Au layer was deposited on quartz substrate by sputtering. Pulsed laser deposition was used to synthesize the CeO_2 thin layer on Au substrate using a KrF excimer laser with a wavelength of 248 nm. The films were deposited at 600 °C under 10 mTorr oxygen pressure. After the growth process, the films were cooled down to room temperature in 2 Torr oxygen pressure to oxidize the films.

To transfer MoS_2 to graphite substrate for STM/STS measurement, water-assisted transfer (PMMA-free) was used. In the process, a PDMS piece about 1 cm^3 with a drop of water was pressed on as-grown MoS_2 on Si/SiO_2 substrate. A small area of MoS_2 was attached to PDMS, which was then pressed on to the target substrate. After removing PDMS, MoS_2 was left clean on the target substrate with no PMMA residues.

XPS Measurements. An Omicron EA 125 hemispherical analyzer and Omicron DAR 400 Mg/Al dual anode nonmonochromatic X-ray source were used for the X-ray photoelectron spectroscopy (XPS) measurements for probing the surface chemistry and core level peaks of MoS_2 on different substrates. Peak-fitting and chemical qualification were performed using the CasaXPS software.

STM/STS Measurements. A variable-temperature scanning tunneling microscope (VT-STM) (Omicron GmbH, Germany) was used to probe the surface morphology and to obtain surface electronic structure information with high spatial resolution at room temperature. STM/STS was performed in UHV (1×10^{-10} mbar) chamber at constant-current mode using W tips. A tip bias voltage of 1.5 V and feedback tunneling current of 50−100 pA was used during the measurements. The tunneling spectra were collected using a lock-in preamplifier to increase the signal-to-noise ratio. For surface cleaning, the samples were annealed in the STM chamber at 350 °C in vacuum for 3 h before STM/STS measurement. For performing STM/STS on MoS_2, HOPG substrate rather than Au/quartz was used, because MoS_2 on HOPG provided higher quality STM/STS data compared to other substrates.

Thermal Annealing and Ion Irradiation of MoS_2. The thermal annealing and ion irradiation were carried out using the direct heating stage and Ar^+ sputtering gun, which were installed in the same UHV chamber as STM/STS and XPS. The Ar^+ ion energy was 500 eV with a fixed emission current of 20 mA.

Raman and PL Spectroscopy Measurements. A Horiba-JY HR 800 system was used to measure the Raman and PL spectra of MoS_2. The 532 nm laser was focused using a 100× objective down to a spot size of 1 μm on the sample surface. The laser power on the sample was

DOI: 10.1021/acsnano.7b08418
ACS Nano 2018, 12, 2569−2579

controlled at 0.5 mW, and a 600 lines/mm grating was used. The Raman and PL peak parameters were obtained by fitting the spectra using Gaussian/Lorentzian line shape.

HER Measurements. The HER measurement was carried out using a three electrode system, using MoS_2 on glassy carbon as the working electrode, carbon rod as the counter electrode, and Ag/AgCl electrode as the reference electrode. 1 M H_2SO_4 was used as the electrolyte. Before each measurement, the cell was purged with Ar for 30 min to remove any residual gas. A Parstat 2273 potentiostat was used to perform the linear sweep measurements with a scan rate of 6 mV/s.

Atomistic Simulations and Electronic Structure Calculations. MD simulations were performed using the large-scale/molecular massively parallel simulator (LAMMPS).[68] Ion irradiations were conducted on a free-standing SL MoS_2. The incident Ar^+ ion was initially placed at 20 Å above the MoS_2 sheet, and the incident direction was perpendicular to the MoS_2 sheet. The incident energies were varied from 50 eV to 1000 keV, and 100 independent simulations were carried out for each specific energy. The first-principles level calculations of the electronic structure were carried out based on the spin-polarized DFT[69] employing periodic boundary conditions as implemented in the Vienna *ab initio* simulation package (VASP).[70,71] The projector augmented wave (PAW)[72,73] pseudopotentials and the generalized gradient approximation (GGA)[74] functional of Perdew, Burke, and Ernzerhof (PBE)[74] were used.

ASSOCIATED CONTENT

Supporting Information

The Supporting Information is available free of charge on the ACS Publications website at DOI: 10.1021/acsnano.7b08418.

Calculation details and supporting figures (PDF)

AUTHOR INFORMATION

Corresponding Authors

*E-mail: escheny@scut.edu.cn.
*E-mail: jingkong@mit.edu.
*E-mail: byildiz@mit.edu.

ORCID

Yan Chen: 0000-0001-6193-7508
Kiran Adepalli: 0000-0001-9641-1901
Xinwei Wang: 0000-0002-1191-8162
Jing Kong: 0000-0003-0551-1208

Present Address

¶Guangzhou Key Laboratory for Surface Chemistry of Energy Materials, New Energy Research Institute, School of Environment and Energy, South China University of Technology, Guangzhou, Guangdong, 510006, China

Author Contributions

●These authors contributed equally to this work. Y.C., S.H., B.Y., and J.K. initiated and designed the project. Y.C. performed the XPS measurements, S.H. performed the PL and Raman spectroscopy measurements, and K.A. performed the STM and STS measurements. X.J. and X.L. performed CVD synthesis of SL graphene and MoS_2. K.Y, X.W., and J.X. performed DFT and MD simulations. All authors discussed the results, analyzed the data, and contributed to the writing of the manuscript.

Notes

The authors declare no competing financial interest.

ACKNOWLEDGMENTS

Y.C. acknowledges the support from Natural Science Foundation of China (11605063), the Schlumberger Foundation Faculty for the Future Fellowship, Guangdong Innovative and Entrepreneurial Research Team Program (2014ZT05N200), the Recruitment Program of Global Youth Experts. S.H., X.L., and M.D. acknowledge a grant DE-SC0001299 for financial support. S.H. acknowledges support from Materials Research Institute and Department of Electrical Engineering at The Pennsylvania State University. K.Y., X.W., and J.X. acknowledge the support from IAEA (CRP no. F11020 and contract no. 21063). X.J. acknowledges support from the Center for Excitonics, an Energy Frontier Research Center funded by the U.S. Department of Energy, Office of Science, Basic Energy Sciences, under award no. DE-SC0001088. J.K. acknowledges support from the Center for Energy Efficient Electronics Science (NSF Award 0939514). B.Y. and Y.C. acknowledge support for this research from the U.S. Department of Energy, Office of Science, Basic Energy Sciences under award no. DE-SC0002633. We acknowledge Wenjing Fang and Yong Cheol Shin for providing CVD grown SLG and SL-BN.

REFERENCES

(1) Radisavljevic, B.; Radenovic, A.; Brivio, J.; Giacometti, V.; Kis, A. Single-Layer MoS2 Transistors. *Nat. Nanotechnol.* **2011**, *6*, 147−150.
(2) Wang, Q. H.; Kalantar-Zadeh, K.; Kis, A.; Coleman, J. N.; Strano, M. S. Electronics and Optoelectronics of Two-Dimensional Transition Metal Dichalcogenides. *Nat. Nanotechnol.* **2012**, *7*, 699−712.
(3) Bertolazzi, S.; Brivio, J.; Kis, A. Stretching and Breaking of Ultrathin MoS2. *ACS Nano* **2011**, *5*, 9703−9709.
(4) Mak, K.; Lee, C.; Hone, J.; Shan, J.; Heinz, T. Atomically Thin MoS2: A New Direct-Gap Semiconductor. *Phys. Rev. Lett.* **2010**, *105*, 2−5.
(5) Huang, S.; Ling, X.; Liang, L.; Kong, J.; Terrones, H.; Meunier, V.; Dresselhaus, M. S. Probing the Interlayer Coupling of Twisted Bilayer MoS2 Using Photoluminescence Spectroscopy. *Nano Lett.* **2014**, *14*, 5500−5508.
(6) Lopez-Sanchez, O.; Lembke, D.; Kayci, M.; Radenovic, A.; Kis, A. Ultrasensitive Photodetectors Based on Monolayer MoS2. *Nat. Nanotechnol.* **2013**, *8*, 497−501.
(7) Huang, S.; Liang, L.; Ling, X.; Puretzky, A. A.; Geohegan, D. B.; Sumpter, B. G.; Kong, J.; Meunier, V.; Dresselhaus, M. S. Low-Frequency Interlayer Raman Modes to Probe Interface of Twisted Bilayer MoS_2. *Nano Lett.* **2016**, *16*, 1435−1444.
(8) Merki, D.; Hu, X. Recent Developments of Molybdenum and Tungsten Sulfides as Hydrogen Evolution Catalysts. *Energy Environ. Sci.* **2011**, *4*, 3878.
(9) Komsa, H.-P.; Kotakoski, J.; Kurasch, S.; Lehtinen, O.; Kaiser, U.; Krasheninnikov, A. V. Two-Dimensional Transition Metal Dichalcogenides under Electron Irradiation: Defect Production and Doping. *Phys. Rev. Lett.* **2012**, *109*, 35503.
(10) Tao, L.; Duan, X.; Wang, C.; Duan, X.; Wang, S. Plasma-Engineered MoS 2 Thin-Film as an Efficient Electrocatalyst for Hydrogen Evolution Reaction. *Chem. Commun.* **2015**, *51*, 7470−7473.
(11) Li, H.; Tsai, C.; Koh, A. L.; Cai, L.; Contryman, A. W.; Fragapane, A. H.; Zhao, J.; Han, H. S.; Manoharan, H. C.; Abild-Pedersen, F.; Nørskov, J. K.; Zheng, X. Activating and Optimizing MoS2 Basal Planes for Hydrogen Evolution through the Formation of Strained Sulphur Vacancies. *Nat. Mater.* **2016**, *15*, 48−53.
(12) Zhou, W.; Zou, X.; Najmaei, S.; Liu, Z.; Shi, Y.; Kong, J.; Lou, J.; Ajayan, P. M.; Yakobson, B. I.; Idrobo, J.-C. Intrinsic Structural Defects in Monolayer Molybdenum Disulfide. *Nano Lett.* **2013**, *13*, 2615−2622.
(13) Han, S. W.; Hwang, Y. H.; Kim, S.-H.; Yun, W. S.; Lee, J. D.; Park, M. G.; Ryu, S.; Park, J. S.; Yoo, D.-H.; Yoon, S.-P.; Hong, S. C.; Kim, K. S.; Park, Y. S. Controlling Ferromagnetic Easy Axis in a Layered MoS2 Single Crystal. *Phys. Rev. Lett.* **2013**, *110*, 247201.
(14) Tongay, S.; Suh, J.; Ataca, C.; Fan, W.; Luce, A.; Kang, J. S.; Liu, J.; Ko, C.; Raghunathanan, R.; Zhou, J.; Ogletree, F.; Li, J.; Grossman, J. C.; Wu, J. Defects Activated Photoluminescence in Two-Dimen-

DOI: 10.1021/acsnano.7b08418
ACS Nano 2018, 12, 2569−2579

sional Semiconductors: Interplay between Bound, Charged and Free Excitons. *Sci. Rep.* **2013**, *3*, 2657.
(15) Le, D.; Rawal, T. B.; Rahman, T. S. Single-Layer MoS_2 with Sulfur Vacancies: Structure and Catalytic Application. *J. Phys. Chem. C* **2014**, *118*, 5346−5351.
(16) McDonnell, S.; Addou, R.; Buie, C.; Wallace, R. M.; Hinkle, C. L. Defect-Dominated Doping and Contact Resistance in MoS_2. *ACS Nano* **2014**, *8*, 2880−2888.
(17) Qiu, H.; Xu, T.; Wang, Z.; Ren, W.; Nan, H.; Ni, Z.; Chen, Q.; Yuan, S.; Miao, F.; Song, F.; Long, G.; Shi, Y.; Sun, L.; Wang, J.; Wang, X. Hopping Transport through Defect-Induced Localized States in Molybdenum Disulphide. *Nat. Commun.* **2013**, *4*, 2643.
(18) Ugeda, M. M.; Bradley, A. J.; Shi, S.-F.; da Jornada, F. H.; Zhang, Y.; Qiu, D. Y.; Ruan, W.; Mo, S.-K.; Hussain, Z.; Shen, Z.-X.; Wang, F.; Louie, S. G.; Crommie, M. F. Giant Giant Bandgap Renormalization and Excitonic Effects in a Monolayer Transition Metal Dichalcogenide Semiconductor. *Nat. Mater.* **2014**, *13*, 1091−1095.
(19) Komsa, H.-P.; Krasheninnikov, A. V. Native Defects in Bulk and Monolayer MoS2 from First Principles. *Phys. Rev. B: Condens. Matter Mater. Phys.* **2015**, *91*, 125304.
(20) Yu, Z. G.; Zhang, Y.-W.; Yakobson, B. I. An Anomalous Formation Pathway for Dislocation-Sulfur Vacancy Complexes in Polycrystalline Monolayer MoS 2. *Nano Lett.* **2015**, *15*, 6855−6861.
(21) Ling, X.; Lee, Y.-H.; Lin, Y.; Fang, W.; Yu, L.; Dresselhaus, M. S.; Kong, J. Role of the Seeding Promoter in MoS2 Growth by Chemical Vapor Deposition. *Nano Lett.* **2014**, *14*, 464−472.
(22) Donarelli, M.; Bisti, F.; Perrozzi, F.; Ottaviano, L. Tunable Sulfur Desorption in Exfoliated MoS_2 by Means of Thermal Annealing in Ultra-High Vacuum. *Chem. Phys. Lett.* **2013**, *588*, 198−202.
(23) Ma, Q.; Isarraraz, M.; Wang, C. S.; Preciado, E.; Klee, V.; Bobek, S.; Yamaguchi, K.; Li, E.; Odenthal, P. M.; Nguyen, A.; Barroso, D.; Sun, D.; von Son Palacio, G.; Gomez, M.; Nguyen, A.; Le, D.; Pawin, G.; Mann, J.; Heinz, T. F.; Rahman, T. S.; Bartels, L. Postgrowth Tuning of the Bandgap of Single-Layer Molybdenum Disulfide Films by Sulfur/Selenium Exchange. *ACS Nano* **2014**, *8*, 4672−4677.
(24) Fox, D. S.; Zhou, Y.; Maguire, P.; O'Neill, A.; Ó'Coileáin, C.; Gatensby, R.; Glushenkov, A. M.; Tao, T.; Duesberg, G. S.; Shvets, I. V.; Abid, M.; Abid, M.; Wu, H.-C.; Chen, Y.; Coleman, J. N.; Donegan, J. F.; Zhang, H. Nanopatterning and Electrical Tuning of MoS 2 Layers with a Subnanometer Helium Ion Beam. *Nano Lett.* **2015**, *15*, 5307−5313.
(25) Ma, Q.; Odenthal, P. M.; Mann, J.; Le, D.; Wang, C. S.; Zhu, Y.; Chen, T.; Sun, D.; Yamaguchi, K.; Tran, T.; Wurch, M.; McKinley, J. L.; Wyrick, J.; Magnone, K.; Heinz, T. F.; Rahman, T. S.; Kawakami, R.; Bartels, L. Controlled Argon Beam-Induced Desulfurization of Monolayer Molybdenum Disulfide. *J. Phys.: Condens. Matter* **2013**, *25*, 252201.
(26) Mathew, S.; Gopinadhan, K.; Chan, T. K.; Yu, X. J.; Zhan, D.; Cao, L.; Rusydi, A.; Breese, M. B. H.; Dhar, S.; Shen, Z. X.; Venkatesan, T.; Thong, J. T. L. Magnetism in MoS2 Induced by Proton Irradiation. *Appl. Phys. Lett.* **2012**, *101*, 102103.
(27) Inoue, A.; Komori, T.; Shudo, K. Atomic-Scale Structures and Electronic States of Defects on Ar+-Ion Irradiated MoS2. *J. Electron Spectrosc. Relat. Phenom.* **2013**, *189*, 11−18.
(28) Mignuzzi, S.; Pollard, A. J.; Bonini, N.; Brennan, B.; Gilmore, I. S.; Pimenta, M. A.; Richards, D.; Roy, D. Effect of Disorder on Raman Scattering of Single-Layer Mo S 2. *Phys. Rev. B: Condens. Matter Mater. Phys.* **2015**, *91*, 195411.
(29) Baker, M.; Gilmore, R.; Lenardi, C.; Gissler, W. XPS Investigation of Preferential Sputtering of S from MoS2 and Determination of MoSx Stoichiometry from Mo and S Peak Positions. *Appl. Surf. Sci.* **1999**, *150*, 255−262.
(30) Bertolazzi, S.; Bonacchi, S.; Nan, G.; Pershin, A.; Beljonne, D.; Samorì, P. Engineering Chemically Active Defects in Monolayer MoS_2 Transistors *via* Ion-Beam Irradiation and Their Healing *via* Vapor Deposition of Alkanethiols. *Adv. Mater.* **2017**, *29*, 1606760.
(31) Pfau, A.; Schierbaum, K. D. The Electronic Structure of Stoichiometric and Reduced CeO2 Surfaces: An XPS, UPS and HREELS Study. *Surf. Sci.* **1994**, *321*, 71−80.
(32) Cumings, J.; Zettl, A. Field Emission and Current-Voltage Properties of Boron Nitride Nanotubes. *Solid State Commun.* **2004**, *129*, 661−664.
(33) Lee, G.-H.; Yu, Y.-J.; Lee, C.; Dean, C.; Shepard, K. L.; Kim, P.; Hone, J. Electron Tunneling through Atomically Flat and Ultrathin Hexagonal Boron Nitride. *Appl. Phys. Lett.* **2011**, *99*, 243114.
(34) Gong, C.; Colombo, L.; Wallace, R. M.; Cho, K. The Unusual Mechanism of Partial Fermi Level Pinning at Metal−MoS 2 Interfaces. *Nano Lett.* **2014**, *14*, 1714−1720.
(35) Coy Diaz, H.; Addou, R.; Batzill, M. Interface Properties of CVD Grown Graphene Transferred onto MoS 2(0001). *Nanoscale* **2014**, *6*, 1071−1078.
(36) Giovannetti, G.; Khomyakov, P. A.; Brocks, G.; Karpan, V. M.; van den Brink, J.; Kelly, P. J. Doping Graphene with Metal Contacts. *Phys. Rev. Lett.* **2008**, *101*, 26803.
(37) Ling, F. L.; Zhou, T. W.; Liu, X. Q.; Kang, W.; Zeng, W.; Zhang, Y. X.; Fang, L.; Lu, Y.; Zhou, M. Electric Field Tuned MoS_2 /metal Interface for Hydrogen Evolution Catalyst from First-Principles Investigations. *Nanotechnology* **2018**, *29*, 03LT01.
(38) Tongay, S.; Fan, W.; Kang, J.; Park, J.; Koldemir, U.; Suh, J.; Narang, D. S.; Liu, K.; Ji, J.; Li, J.; Sinclair, R.; Wu, J. Tuning Interlayer Coupling in Large-Area Heterostructures with CVD-Grown MoS 2 and WS 2 Monolayers. *Nano Lett.* **2014**, *14*, 3185−3190.
(39) Terrones, H.; López-Urías, F.; Terrones, M. Novel Hetero-Layered Materials with Tunable Direct Band Gaps by Sandwiching Different Metal Disulfides and Diselenides. *Sci. Rep.* **2013**, *3*, 1549.
(40) Chakraborty, B.; Bera, A.; Muthu, D. V. S.; Bhowmick, S.; Waghmare, U. V.; Sood, A. K. Symmetry-Dependent Phonon Renormalization in Monolayer MoS_2 Transistor. *Phys. Rev. B: Condens. Matter Mater. Phys.* **2012**, *85*, 161403.
(41) Sercombe, D.; Schwarz, S.; Pozo-Zamudio, O. D.; Liu, F.; Robinson, B. J.; Chekhovich, E. A.; Tartakovskii, I. I.; Kolosov, O.; Tartakovskii, A. I. Optical Investigation of the Natural Electron Doping in Thin MoS_2 Films Deposited on Dielectric Substrates. *Sci. Rep.* **2013**, *3*, 3489.
(42) Conley, H. J.; Wang, B.; Ziegler, J. I.; Haglund, R. F.; Pantelides, S. T.; Bolotin, K. I. Bandgap Engineering of Strained Monolayer and Bilayer MoS_2. *Nano Lett.* **2013**, *13*, 3626−3630.
(43) Tuller, H. L.; Bishop, S. R. Point Defects in Oxides: Tailoring Materials Through Defect Engineering. *Annu. Rev. Mater. Res.* **2011**, *41*, 369−398.
(44) Zacherle, T.; Schriever, A.; De Souza, R. A.; Martin, M. Ab Initio Analysis of the Defect Structure of Ceria. *Phys. Rev. B: Condens. Matter Mater. Phys.* **2013**, *87*, 134104.
(45) Feng, Z. A.; Balaji Gopal, C.; Ye, X.; Guan, Z.; Jeong, B.; Crumlin, E.; Chueh, W. C. Origin of Overpotential-Dependent Surface Dipole at CeO_{2-X} /Gas Interface During Electrochemical Oxygen Insertion Reactions. *Chem. Mater.* **2016**, *28*, 6233−6242.
(46) Mullins, D.; Overbury, S.; Huntley, D. Electron Spectroscopy of Single Crystal and Polycrystalline Cerium Oxide Surfaces. *Surf. Sci.* **1998**, *409*, 307−319.
(47) Chueh, W. C.; McDaniel, A. H.; Grass, M. E.; Hao, Y.; Jabeen, N.; Liu, Z.; Haile, S. M.; McCarty, K. F.; Bluhm, H.; El Gabaly, F. Highly Enhanced Concentration and Stability of Reactive Ce^{3+} on Doped CeO_2 Surface Revealed In Operando. *Chem. Mater.* **2012**, *24*, 1876−1882.
(48) Wang, Y.-G.; Mei, D.; Li, J.; Rousseau, R. DFT+U Study on the Localized Electronic States and Their Potential Role During H_2O Dissociation and CO Oxidation Processes on CeO_2 (111). *J. Phys. Chem. C* **2013**, *117*, 23082−23089.
(49) Su, Y.-Q.; Filot, I. A. W.; Liu, J.-X.; Tranca, I.; Hensen, E. J. M. Charge Transport over the Defective CeO_2 (111). *Chem. Mater.* **2016**, *28*, 5652−5658.
(50) Madauß, L.; Ochedowski, O.; Lebius, H.; Ban-d'Etat, B.; Naylor, C. H.; Johnson, A. T. C.; Kotakoski, J.; Schleberger, M. Defect

DOI: 10.1021/acsnano.7b08418
ACS Nano 2018, 12, 2569−2579

Engineering of Single- and Few-Layer MoS 2 by Swift Heavy Ion Irradiation. *2D Mater.* **2017**, *4*, 15034.
(51) He, K.; Poole, C.; Mak, K. F.; Shan, J. Experimental Demonstration of Continuous Electronic Structure Tuning *via* Strain in Atomically Thin MoS_2. *Nano Lett.* **2013**, *13*, 2931−2936.
(52) Ryou, J.; Kim, Y.-S.; KC, S.; Cho, K. Monolayer MoS_2 Bandgap Modulation by Dielectric Environments and Tunable Bandgap Transistors. *Sci. Rep.* **2016**, *6*, 29184.
(53) Huang, Y. L.; Chen, Y.; Zhang, W.; Quek, S. Y.; Chen, C.-H.; Li, L.-J.; Hsu, W.-T.; Chang, W.-H.; Zheng, Y. J.; Chen, W.; Wee, A. T. S. Bandgap Tunability at Single-Layer Molybdenum Disulphide Grain Boundaries. *Nat. Commun.* **2015**, *6*, 6298.
(54) Li, H.; Contryman, A. W.; Qian, X.; Ardakani, S. M.; Gong, Y.; Wang, X.; Weisse, J. M.; Lee, C. H.; Zhao, J.; Ajayan, P. M.; Li, J.; Manoharan, H. C.; Zheng, X. Optoelectronic Crystal of Artificial Atoms in Strain-Textured Molybdenum Disulphide. *Nat. Commun.* **2015**, *6*, 7381.
(55) Zhang, C.; Johnson, A.; Hsu, C.-L.; Li, L.-J.; Shih, C.-K. Direct Imaging of Band Profile in Single Layer MoS_2 on Graphite: Quasiparticle Energy Gap, Metallic Edge States, and Edge Band Bending. *Nano Lett.* **2014**, *14*, 2443−2447.
(56) Lu, C.-P.; Li, G.; Mao, J.; Wang, L.-M.; Andrei, E. Y. Bandgap, Mid-Gap States, and Gating Effects in MoS_2. *Nano Lett.* **2014**, *14*, 4628−4633.
(57) Tongay, S.; Suh, J.; Ataca, C.; Fan, W.; Luce, A.; Kang, J. S.; Liu, J.; Ko, C.; Raghunathanan, R.; Zhou, J.; Ogletree, F.; Li, J.; Grossman, J. C.; Wu, J. Defects Activated Photoluminescence in Two-Dimensional Semiconductors: Interplay between Bound, Charged, and Free Excitons. *Sci. Rep.* **2013**, *3*, 2657.
(58) Li, H.; Huang, M.; Cao, G. Markedly Different Adsorption Behaviors of Gas Molecules on Defective Monolayer MoS_2 : A First-Principles Study. *Phys. Chem. Chem. Phys.* **2016**, *18*, 15110−15117.
(59) Li, G.; Zhang, D.; Qiao, Q.; Yu, Y.; Peterson, D.; Zafar, A.; Kumar, R.; Curtarolo, S.; Hunte, F.; Shannon, S.; Zhu, Y.; Yang, W.; Cao, L. All The Catalytic Active Sites of MoS 2 for Hydrogen Evolution. *J. Am. Chem. Soc.* **2016**, *138*, 16632−16638.
(60) Lopez-Sanchez, O.; Alarcon Llado, E.; Koman, V.; Fontcuberta i Morral, A.; Radenovic, A.; Kis, A. Light Generation and Harvesting in a van Der Waals Heterostructure. *ACS Nano* **2014**, *8*, 3042−3048.
(61) Dhyani, V.; Das, S. High-Speed Scalable Silicon-MoS2 P-N Heterojunction Photodetectors. *Sci. Rep.* **2017**, *7*, 44243.
(62) Tsuboi, Y.; Wang, F.; Kozawa, D.; Funahashi, K.; Mouri, S.; Miyauchi, Y.; Takenobu, T.; Matsuda, K. Enhanced Photovoltaic Performances of graphene/Si Solar Cells by Insertion of a MoS_2 Thin Film. *Nanoscale* **2015**, *7*, 14476−14482.
(63) Sarkar, D.; Xie, X.; Liu, W.; Cao, W.; Kang, J.; Gong, Y.; Kraemer, S.; Ajayan, P. M.; Banerjee, K. A Subthermionic Tunnel Field-Effect Transistor with an Atomically Thin Channel. *Nature* **2015**, *526*, 91−95.
(64) Li, X.-X.; Fan, Z.-Q.; Liu, P.-Z.; Chen, M.-L.; Liu, X.; Jia, C.-K.; Sun, D.-M.; Jiang, X.-W.; Han, Z.; Bouchiat, V.; Guo, J.-J.; Chen, J.-H.; Zhang, Z.-D. Gate-Controlled Reversible Rectifying Behaviour in Tunnel Contacted Atomically-Thin MoS2 Transistor. *Nat. Commun.* **2017**, *8*, 970.
(65) Li, X.; Cai, W.; An, J.; Kim, S.; Nah, J.; Yang, D.; Piner, R.; Velamakanni, A.; Jung, I.; Tutuc, E.; Banerjee, S. K.; Colombo, L.; Ruoff, R. S. Large-Area Synthesis of High-Quality and Uniform Graphene Films on Copper Foils. *Science* **2009**, *324*, 1312−1314.
(66) Reina, A.; Jia, X.; Ho, J.; Nezich, D.; Son, H.; Bulovic, V.; Dresselhaus, M. S.; Kong, J. Large Area, Few-Layer Graphene Films on Arbitrary Substrates by Chemical Vapor Deposition. *Nano Lett.* **2009**, *9*, 30−35.
(67) Kim, K. K.; Hsu, A.; Jia, X.; Kim, S. M.; Shi, Y.; Hofmann, M.; Nezich, D.; Rodriguez-Nieva, J. F.; Dresselhaus, M.; Palacios, T.; Kong, J. Synthesis of Monolayer Hexagonal Boron Nitride on Cu Foil Using Chemical Vapor Deposition. *Nano Lett.* **2012**, *12*, 161−166.
(68) Khare, K. S.; Khare, R. Directed Diffusion Approach for Preparing Atomistic Models of Crosslinked Epoxy for Use in Molecular Simulations. Macromol. *Macromol. Theory Simul.* **2012**, *21*, 322−327.
(69) Hohenberg, P.; Kohn, W. Inhomogeneous Electron Gas. *Phys. Rev.* **1964**, *136*, B864−B871.
(70) Kresse, G.; Furthmüller, J. Efficiency of Ab-Initio Total Energy Calculations for Metals and Semiconductors Using a Plane-Wave Basis Set. *Comput. Mater. Sci.* **1996**, *6*, 15−50.
(71) Kresse, G.; Furthmüller, J. Efficient Iterative Schemes for Ab Initio Total-Energy Calculations Using a Plane-Wave Basis Set. *Phys. Rev. B: Condens. Matter Mater. Phys.* **1996**, *54*, 11169−11186.
(72) Blöchl, P. E. Projector Augmented-Wave Method. *Phys. Rev. B: Condens. Matter Mater. Phys.* **1994**, *50*, 17953−17979.
(73) Kresse, G.; Joubert, D. From Ultrasoft Pseudopotentials to the Projector Augmented-Wave Method. *Phys. Rev. B: Condens. Matter Mater. Phys.* **1999**, *59*, 1758−1775.
(74) Perdew, J. P.; Burke, K.; Ernzerhof, M. Generalized Gradient Approximation Made Simple. *Phys. Rev. Lett.* **1996**, *77*, 3865−3868.

DOI: 10.1021/acsnano.7b08418
ACS Nano 2018, 12, 2569−2579